Measurement of inclusive J/ψ polarization in $p+p$ collisions at $\sqrt{s}=200$ GeV by the STAR experiment

J. Adam,[6] L. Adamczyk,[2] J. R. Adams,[39] J. K. Adkins,[30] G. Agakishiev,[28] M. M. Aggarwal,[42] Z. Ahammed,[61] I. Alekseev,[3,35] D. M. Anderson,[55] A. Aparin,[28] E. C. Aschenauer,[6] M. U. Ashraf,[11] F. G. Atetalla,[29] A. Attri,[42] G. S. Averichev,[28] V. Bairathi,[22] K. Barish,[10] A. Behera,[53] R. Bellwied,[20] A. Bhasin,[27] J. Bielcik,[14] J. Bielcikova,[38] L. C. Bland,[6] I. G. Bordyuzhin,[3] J. D. Brandenburg,[50,6] A. V. Brandin,[35] S. Bueltmann,[40] J. Butterworth,[46] H. Caines,[64] M. Calderón de la Barca Sánchez,[8] D. Cebra,[8] I. Chakaberia,[29,6] P. Chaloupka,[14] B. K. Chan,[9] F-H. Chang,[37] Z. Chang,[6] N. Chankova-Bunzarova,[28] A. Chatterjee,[11] D. Chen,[10] J. H. Chen,[18] X. Chen,[49] Z. Chen,[50] J. Cheng,[57] M. Cherney,[13] M. Chevalier,[10] S. Choudhury,[18] W. Christie,[6] H. J. Crawford,[7] M. Csanád,[16] M. Daugherity,[1] T. G. Dedovich,[28] I. M. Deppner,[19] A. A. Derevschikov,[44] L. Didenko,[6] X. Dong,[31] J. L. Drachenberg,[1] J. C. Dunlop,[6] T. Edmonds,[45] N. Elsey,[63] J. Engelage,[7] G. Eppley,[46] R. Esha,[53] S. Esumi,[58] O. Evdokimov,[12] A. Ewigleben,[32] O. Eyser,[6] R. Fatemi,[30] S. Fazio,[6] P. Federic,[38] J. Fedorisin,[28] C. J. Feng,[37] Y. Feng,[45] P. Filip,[28] E. Finch,[52] Y. Fisyak,[6] A. Francisco,[64] L. Fulek,[2] C. A. Gagliardi,[55] T. Galatyuk,[15] F. Geurts,[46] A. Gibson,[60] K. Gopal,[23] D. Grosnick,[60] W. Guryn,[6] A. I. Hamad,[29] A. Hamed,[5] J. W. Harris,[64] S. He,[11] W. He,[18] X. He,[26] S. Heppelmann,[8] S. Heppelmann,[43] N. Herrmann,[19] E. Hoffman,[20] L. Holub,[14] Y. Hong,[31] S. Horvat,[64] Y. Hu,[18] H. Z. Huang,[9] S. L. Huang,[53] T. Huang,[37] X. Huang,[57] T. J. Humanic,[39] P. Huo,[53] G. Igo,[9] D. Isenhower,[1] W. W. Jacobs,[25] C. Jena,[23] A. Jentsch,[6] Y. JI,[49] J. Jia,[6,53] K. Jiang,[49] S. Jowzaee,[63] X. Ju,[49] E. G. Judd,[7] S. Kabana,[29] M. L. Kabir,[10] S. Kagamaster,[32] D. Kalinkin,[25] K. Kang,[57] D. Kapukchyan,[10] K. Kauder,[6] H. W. Ke,[6] D. Keane,[29] A. Kechechyan,[28] M. Kelsey,[31] Y. V. Khyzhniak,[35] D. P. Kikoła,[62] C. Kim,[10] B. Kimelman,[8] D. Kincses,[16] T. A. Kinghorn,[8] I. Kisel,[17] A. Kiselev,[6] A. Kisiel,[62] M. Kocan,[14] L. Kochenda,[35] L. K. Kosarzewski,[14] L. Kramarik,[14] P. Kravtsov,[35] K. Krueger,[4] N. Kulathunga Mudiyanselage,[20] L. Kumar,[42] R. Kunnawalkam Elayavalli,[63] J. H. Kwasizur,[25] R. Lacey,[53] S. Lan,[11] J. M. Landgraf,[6] J. Lauret,[6] A. Lebedev,[6] R. Lednicky,[28] J. H. Lee,[6] Y. H. Leung,[31] C. Li,[49] W. Li,[46] W. Li,[51] X. Li,[49] Y. Li,[57] Y. Liang,[29] R. Licenik,[38] T. Lin,[55] Y. Lin,[11] M. A. Lisa,[39] F. Liu,[11] H. Liu,[25] P. Liu,[53] P. Liu,[51] T. Liu,[64] X. Liu,[39] Y. Liu,[55] Z. Liu,[49] T. Ljubicic,[6] W. J. Llope,[63] R. S. Longacre,[6] N. S. Lukow,[54] S. Luo,[12] X. Luo,[11] G. L. Ma,[51] L. Ma,[18] R. Ma,[6] Y. G. Ma,[51] N. Magdy,[12] R. Majka,[64] D. Mallick,[36] S. Margetis,[29] C. Markert,[56] H. S. Matis,[31] J. A. Mazer,[47] N. G. Minaev,[44] S. Mioduszewski,[55] B. Mohanty,[36] M. M. Mondal,[53] I. Mooney,[63] Z. Moravcova,[14] D. A. Morozov,[44] M. Nagy,[16] J. D. Nam,[54] Md. Nasim,[22] K. Nayak,[11] D. Neff,[9] J. M. Nelson,[7] D. B. Nemes,[64] M. Nie,[5] G. Nigmatkulov,[35] T. Niida,[58] L. V. Nogach,[44] T. Nonaka,[58] G. Odyniec,[31] A. Ogawa,[6] S. Oh,[31] V. A. Okorokov,[35] B. S. Page,[6] R. Pak,[6] A. Pandav,[36] Y. Panebratsev,[28] B. Pawlik,[41] D. Pawlowska,[62] H. Pei,[11] C. Perkins,[7] L. Pinsky,[20] R. L. Pintér,[16] J. Pluta,[62] J. Porter,[31] M. Posik,[54] N. K. Pruthi,[42] M. Przybycien,[2] J. Putschke,[63] H. Qiu,[26] A. Quintero,[54] S. K. Radhakrishnan,[59] S. Ramachandran,[30] R. L. Ray,[56] R. Reed,[32] H. G. Ritter,[31] J. B. Roberts,[46] O. V. Rogachevskiy,[28] J. L. Romero,[8] L. Ruan,[6] J. Rusnak,[38] N. R. Sahoo,[50] H. Sako,[58] S. Salur,[47] J. Sandweiss,[64] S. Sato,[58] W. B. Schmidke,[6] N. Schmitz,[33] B. R. Schweid,[53] F. Seck,[15] J. Seger,[13] M. Sergeeva,[9] R. Seto,[10] P. Seyboth,[33] N. Shah,[24] E. Shahaliev,[28] P. V. Shanmuganathan,[6] M. Shao,[49] F. Shen,[50] W. Q. Shen,[51] S. S. Shi,[11] Q. Y. Shou,[51] E. P. Sichtermann,[31] R. Sikora,[2] M. Simko,[38] J. Singh,[42] S. Singha,[26] N. Smirnov,[64] W. Solyst,[25] P. Sorensen,[6] H. M. Spinka,[4] B. Srivastava,[45] T. D. S. Stanislaus,[60] M. Stefaniak,[62] D. J. Stewart,[64] M. Strikhanov,[35] B. Stringfellow,[45] A. A. P. Suaide,[48] M. Sumbera,[38] B. Summa,[43] X. M. Sun,[11] Y. Sun,[49] Y. Sun,[21] B. Surrow,[54] D. N. Svirida,[3] P. Szymanski,[62] A. H. Tang,[6] Z. Tang,[49] A. Taranenko,[35] T. Tarnowsky,[34] J. H. Thomas,[31] A. R. Timmins,[20] D. Tlusty,[13] M. Tokarev,[28] C. A. Tomkiel,[32] S. Trentalange,[9] R. E. Tribble,[55] P. Tribedy,[6] S. K. Tripathy,[16] O. D. Tsai,[9] Z. Tu,[6] T. Ullrich,[6] D. G. Underwood,[4] I. Upsal,[50,6] G. Van Buren,[6] J. Vanek,[38] A. N. Vasiliev,[44] I. Vassiliev,[17] F. Videbæk,[6] S. Vokal,[28] S. A. Voloshin,[63] F. Wang,[45] G. Wang,[9] J. S. Wang,[21] P. Wang,[49] Y. Wang,[11] Y. Wang,[57] Z. Wang,[50] J. C. Webb,[6] P. C. Weidenkaff,[19] L. Wen,[9] G. D. Westfall,[34] H. Wieman,[31] S. W. Wissink,[25] R. Witt,[59] Y. Wu,[10] Z. G. Xiao,[57] G. Xie,[31] W. Xie,[45] H. Xu,[21] N. Xu,[31] Q. H. Xu,[50] Y. F. Xu,[51] Y. Xu,[50] Z. Xu,[6] Z. Xu,[9] C. Yang,[50] Q. Yang,[50] S. Yang,[6] Y. Yang,[37] Z. Yang,[11] Z. Ye,[46] Z. Ye,[12] L. Yi,[50] K. Yip,[6] H. Zbroszczyk,[62] W. Zha,[49] D. Zhang,[11] S. Zhang,[49] S. Zhang,[51] X. P. Zhang,[57] Y. Zhang,[49] Y. Zhang,[11] Z. J. Zhang,[37] Z. Zhang,[6] Z. Zhang,[12] J. Zhao,[45] C. Zhong,[51] C. Zhou,[51] X. Zhu,[57] Z. Zhu,[50] M. Zurek,[31] and M. Zyzak[17]

(STAR Collaboration)

[1]*Abilene Christian University, Abilene, Texas 79699*
[2]*AGH University of Science and Technology, FPACS, Cracow 30-059, Poland*
[3]*Alikhanov Institute for Theoretical and Experimental Physics NRC "Kurchatov Institute", Moscow 117218, Russia*
[4]*Argonne National Laboratory, Argonne, Illinois 60439*

[5]*American University of Cairo, New Cairo 11835, New Cairo, Egypt*
[6]*Brookhaven National Laboratory, Upton, New York 11973*
[7]*University of California, Berkeley, California 94720*
[8]*University of California, Davis, California 95616*
[9]*University of California, Los Angeles, California 90095*
[10]*University of California, Riverside, California 92521*
[11]*Central China Normal University, Wuhan, Hubei 430079*
[12]*University of Illinois at Chicago, Chicago, Illinois 60607*
[13]*Creighton University, Omaha, Nebraska 68178*
[14]*Czech Technical University in Prague, FNSPE, Prague 115 19, Czech Republic*
[15]*Technische Universität Darmstadt, Darmstadt 64289, Germany*
[16]*ELTE Eötvös Loránd University, Budapest H-1117, Hungary*
[17]*Frankfurt Institute for Advanced Studies FIAS, Frankfurt 60438, Germany*
[18]*Fudan University, Shanghai 200433*
[19]*University of Heidelberg, Heidelberg 69120, Germany*
[20]*University of Houston, Houston, Texas 77204*
[21]*Huzhou University, Huzhou, Zhejiang 313000*
[22]*Indian Institute of Science Education and Research (IISER), Berhampur 760010, India*
[23]*Indian Institute of Science Education and Research (IISER) Tirupati, Tirupati 517507, India*
[24]*Indian Institute Technology, Patna, Bihar 801106, India*
[25]*Indiana University, Bloomington, Indiana 47408*
[26]*Institute of Modern Physics, Chinese Academy of Sciences, Lanzhou, Gansu 730000*
[27]*University of Jammu, Jammu 180001, India*
[28]*Joint Institute for Nuclear Research, Dubna 141 980, Russia*
[29]*Kent State University, Kent, Ohio 44242*
[30]*University of Kentucky, Lexington, Kentucky 40506-0055*
[31]*Lawrence Berkeley National Laboratory, Berkeley, California 94720*
[32]*Lehigh University, Bethlehem, Pennsylvania 18015*
[33]*Max-Planck-Institut für Physik, Munich 80805, Germany*
[34]*Michigan State University, East Lansing, Michigan 48824*
[35]*National Research Nuclear University MEPhI, Moscow 115409, Russia*
[36]*National Institute of Science Education and Research, HBNI, Jatni 752050, India*
[37]*National Cheng Kung University, Tainan 70101*
[38]*Nuclear Physics Institute of the CAS, Rez 250 68, Czech Republic*
[39]*Ohio State University, Columbus, Ohio 43210*
[40]*Old Dominion University, Norfolk, Virginia 23529*
[41]*Institute of Nuclear Physics PAN, Cracow 31-342, Poland*
[42]*Panjab University, Chandigarh 160014, India*
[43]*Pennsylvania State University, University Park, Pennsylvania 16802*
[44]*NRC "Kurchatov Institute", Institute of High Energy Physics, Protvino 142281, Russia*
[45]*Purdue University, West Lafayette, Indiana 47907*
[46]*Rice University, Houston, Texas 77251*
[47]*Rutgers University, Piscataway, New Jersey 08854*
[48]*Universidade de São Paulo, São Paulo 05314-970, Brazil*
[49]*University of Science and Technology of China, Hefei, Anhui 230026*
[50]*Shandong University, Qingdao, Shandong 266237*
[51]*Shanghai Institute of Applied Physics, Chinese Academy of Sciences, Shanghai 201800*
[52]*Southern Connecticut State University, New Haven, Connecticut 06515*
[53]*State University of New York, Stony Brook, New York 11794*
[54]*Temple University, Philadelphia, Pennsylvania 19122*
[55]*Texas A&M University, College Station, Texas 77843*
[56]*University of Texas, Austin, Texas 78712*
[57]*Tsinghua University, Beijing 100084*
[58]*University of Tsukuba, Tsukuba, Ibaraki 305-8571, Japan*
[59]*United States Naval Academy, Annapolis, Maryland 21402*
[60]*Valparaiso University, Valparaiso, Indiana 46383*
[61]*Variable Energy Cyclotron Centre, Kolkata 700064, India*
[62]*Warsaw University of Technology, Warsaw 00-661, Poland*
[63]*Wayne State University, Detroit, Michigan 48201*
[64]*Yale University, New Haven, Connecticut 06520*

(Received 9 July 2020; accepted 12 October 2020; published 20 November 2020)

We report on new measurements of inclusive J/ψ polarization at midrapidity in $p+p$ collisions at $\sqrt{s}=200$ GeV by the STAR experiment at the Relativistic Heavy Ion Collider. The polarization parameters, λ_θ, λ_ϕ, and $\lambda_{\theta\phi}$, are measured as a function of transverse momentum (p_{T}) in both the helicity and Collins-Soper (CS) reference frames within $p_{\mathrm{T}}<10$ GeV/c. Except for λ_θ in the CS frame at the highest measured p_{T}, all three polarization parameters are consistent with 0 in both reference frames without any strong p_{T} dependence. Several model calculations are compared with data, and the one using the Color Glass Condensate effective field theory coupled with nonrelativistic QCD gives the best overall description of the experimental results, even though other models cannot be ruled out due to experimental uncertainties.

DOI: 10.1103/PhysRevD.102.092009

I. INTRODUCTION

The J/ψ meson, a bound state of a charm (c) and an anticharm ($\bar{c}$) quark, provides a natural testing ground for studying both the perturbative and nonperturbative aspects of QCD. Due to their large masses, the production cross section of $c\bar{c}$ pairs can be calculated perturbatively. On the other hand, the formation of J/ψ mesons from $c\bar{c}$ pairs happens over long distances, and therefore is nonperturbative. The J/ψ mesons are also widely used in heavy-ion physics as an internal probe to study the properties of the quark-gluon plasma [1], which requires the measurement of the J/ψ production in vacuum as a reference. Despite decades of concentrated experimental and theoretical efforts, a complete picture of the J/ψ production mechanism in elementary collisions has yet to emerge.

Model calculations describing the J/ψ production utilize the factorization of the short-distance $c\bar{c}$ production and the long-distance hadronization process [2]. Models differ mainly in the treatment of the nonperturbative formation of J/ψ. One of the early models is the Color Evaporation Model [3,4], which is based on the principle of quark-hadron duality and satisfies all-order factorization. It assumes that every $c\bar{c}$ pair, with an invariant mass below twice the D-meson threshold, evolves into a J/ψ meson with a fixed probability ($F_{J/\psi}$) by randomly emitting or exchanging soft gluons with other color sources. The nonperturbative J/ψ formation is incorporated into the universal probability $F_{J/\psi}$, which is independent of the kinematics and spin of the J/ψ meson. An Improved Color Evaporation Model (ICEM) has recently been proposed, in which the lower limit of the $c\bar{c}$ pair invariant mass is increased to be the charmonium mass and the transverse momentum (p_{T}) of the charmonium state is adjusted based on the ratio of its mass to the $c\bar{c}$ mass [5]. The ICEM calculation is in general agreement with the inclusive J/ψ cross section measured in $p+p$ collisions at $\sqrt{s}=200$ GeV [5], in which the discrepancy seen above $J/\psi\, p_{\mathrm{T}}\sim 4$ GeV/c is mainly due to the missing contribution of b-hadron decays in ICEM. By summing with the contribution of J/ψ from b-hadron decays obtained from the fixed-order plus next-to-leading-logarithm calculation [6], the ICEM calculation agrees reasonably well with the inclusive J/ψ cross section measured in $p+p$ collisions at $\sqrt{s}=500$ GeV [7] up to $p_{\mathrm{T}}^{J/\psi}=20$ GeV/c. A further extension based on ICEM at leading order is the calculation of J/ψ polarization utilizing the k_T-factorization approach [8]. Compared to the measured J/ψ polarization at forward rapidity in $p+p$ collisions at $\sqrt{s}=7$ TeV [9,10], the ICEM calculation shows significant discrepancies at low p_{T}.

A more sophisticated way to describe the hadronization of heavy quarkonia is based on the effective quantum field theory of nonrelativistic QCD (NRQCD) [11]. In addition to the usual expansion in the strong coupling constant (α_s), it also introduces an expansion in the relative velocity between the heavy quarks in the pair. Both the color-singlet and color-octet intermediate $c\bar{c}$ pairs are included in the NRQCD. The hadronization process is incorporated through the assumed universal Long Distance Matrix Elements (LDMEs), which weight the relative contributions of each intermediate state and are extracted from fitting experimental data. The NRQCD calculations at next-to-leading order (NLO) in α_s have been done by three groups [12–14]. They obtained very different LDMEs depending on the low-p_{T} cuts imposed on data points used and whether the polarization data are included. None of these calculations can give a simultaneous description of both the charmonium cross section, such as the η_c yields measured in 7 TeV $p+p$ collisions [15], and polarization such as those measured by the CDF Collaboration [16,17]. To remedy the issue of calculating the $c\bar{c}$ production cross section at low p_{T}, where the collinear factorization formalism may not be applicable, an effort has been made to use the Color Glass Condensate (CGC) effective field theory [18]. Combined with the NRQCD, it

describes well the J/ψ cross sections measured in $p+p$ collisions at both the Relativistic Heavy Ion Collider (RHIC) and the LHC [19]. The CGC + NRQCD formalism has also been used to calculate the J/ψ polarization, and the results agree well with the LHC measurements at forward rapidities [20]. Continued efforts from both experimental and theoretical sides are still needed to achieve the final goal of a complete understanding of J/ψ production.

While the J/ψ production cross section has been measured extensively in $p+p$ collisions at $\sqrt{s}=200$ GeV at RHIC [21–23], its polarization, which is the topic of this paper, is less so [21,24]. The J/ψ polarization can be measured through the angular distribution of the positively charged daughter lepton [25],

$$W(\cos\theta,\phi) \propto \frac{1}{3+\lambda_\theta}(1+\lambda_\theta\cos^2\theta+\lambda_\phi\sin^2\theta\cos 2\phi + \lambda_{\theta\phi}\sin 2\theta\cos\phi), \quad (1)$$

where λ_θ, λ_ϕ and $\lambda_{\theta\phi}$ are the J/ψ polarization parameters. θ and ϕ are the polar and azimuthal angles of the positively charged daughter lepton in the J/ψ rest frame with respect to a chosen quantization axis. In the helicity (HX) frame [26], one uses the opposite of the direction of motion of the interaction point in the J/ψ rest frame as the quantization axis. In the Collins-Soper (CS) frame [27], one chooses the bisector of the angle formed by one beam direction and the opposite direction of the other beam in the J/ψ rest frame. J/ψ is considered fully transversely or longitudinally polarized when the polarization parameters take the values of $(\lambda_\theta,\lambda_\phi,\lambda_{\theta\phi})=(1,0,0)$ or $(-1,0,0)$. No polarization is referred to the case of (0, 0, 0). While the measured polarization values depend on the selection of the quantization axis, one can construct a frame invariant quantity to check the consistency of measurements in different frames [28]. It is defined as

$$\lambda_{\rm inv}=\frac{\lambda_\theta+3\lambda_\phi}{1-\lambda_\phi}. \quad (2)$$

Previous measurements of inclusive J/ψ polarization in 200 GeV $p+p$ collisions [21,24] have only focused on λ_θ in the HX frame within $p_{\rm T}<6$ GeV/c. In this paper, we extend the scope by measuring all three polarization parameters in both HX and CS frames for $p_{\rm T}<10$ GeV/c, as well as the frame invariant quantity $\lambda_{\rm inv}$. Measurements are carried out based on both the dimuon and dielectron decay channels covering different kinematic ranges. The inclusive J/ψ sample used in this paper includes directly produced J/ψ's and those from decays of excited charmonium states such as χ_c and $\psi(2S)$ (approximately 40% [29]) as well as b hadrons (approximately 10%–25% above $p_{\rm T}$ of 5 GeV/c [22]). These measurements will provide more stringent tests of different model calculations, especially for the universality of model parameters, such as $F_{J/\psi}$, LDMEs, that give models their predictive power.

This paper is arranged as the following. An introduction to the Solenoidal Tracker At RHIC (STAR) is given in Sec. II, followed by detailed descriptions of the analyses utilizing the electron and muon decay channels in Secs. III and IV, respectively. The J/ψ polarization results are presented in Sec. V, and a summary is given in Sec. VI.

II. STAR EXPERIMENT

The STAR experiment [30] at RHIC consists of a suite of midrapidity detectors with excellent tracking and particle identification (PID) capabilities. The Time Projection Chamber (TPC) [31] is a gaseous drift chamber with the readout system based on the Multi-Wire Proportional Chambers technology. It is the main tracking device to measure a particle's momentum and specific energy loss (dE/dx) for particle identification and covers the pseudorapidity range of $|\eta|<1$ over full azimuthal angle. A room temperature solenoidal magnet generates a uniform magnetic field of maximum value 0.5 T [32]. The Barrel Electromagnetic Calorimeter (BEMC) [33] is a sampling calorimeter using lead and plastic scintillator. It is used to identify and trigger on high-$p_{\rm T}$ electrons over full azimuthal angle within $|\eta|<1$. In conjunction with the start time provided by the Vertex Position Detector (VPD), the Time-Of-Flight (TOF) detector [34] measures a particle's flight time to further improve the electron purity. For the muon channel analysis, the Muon Telescope Detector (MTD) [35] is used for triggering on and identifying muons. It resides outside of the magnet, which acts as an absorber, and covers about 45% in azimuth within $|\eta|<0.5$. Both the TOF and the MTD utilize the Multi-Gap Resistive Plate Chamber technology. Forward-rapidity trigger detectors, the VPD at $4.24<|\eta|<5.1$ [36] and Beam-Beam Counters at $3.3<|\eta|<5.0$ [37], are used to select collisions.

III. $J/\psi\to e^+e^-$

A. Dataset, event, and track selections

The dataset was taken for $p+p$ collisions at $\sqrt{s}=200$ GeV in 2012 using both the minimum-bias (MB) and high-tower (HT) triggers. The prescaled MB trigger selects nonsingle diffractive $p+p$ collisions with a coincidence signal from the VPD on east and west sides, while the HT trigger selects events with energy depositions in the BEMC above given thresholds. About 300 million MB events, corresponding to an integrated luminosity of about 10 nb^{-1}, are analyzed to study the J/ψ polarization below $p_{\rm T}$ of 2 GeV/c. Data collected by the HT0 (HT2) trigger with an energy threshold of $E_{\rm T}>2.6$ (4.2) GeV correspond to an integrated luminosity of 1.36 (23.5) pb^{-1}. The HT0 trigger is used for the J/ψ measurement within $2<p_{\rm T}<4$ GeV/c, while the HT2 trigger is used for $4<p_{\rm T}<14$ GeV/c.

The vertex position along the beam direction can be reconstructed from TPC tracks (V_z^{TPC}) or from the time difference of east and west VPD signals (V_z^{VPD}). A cut of $|V_z^{\mathrm{TPC}}| < 50$ cm is applied to ensure good TPC acceptance for all the events. An additional cut of $|V_z^{\mathrm{TPC}} - V_z^{\mathrm{VPD}}| < 6$ cm is applied to reduce the pileup background from out-of-time collisions for MB events.

Charged tracks are required to have at least 20 TPC space points (out of a maximum of 45), a ratio of at least 0.52 between actually used and maximum possible number of TPC space points, at least 11 TPC space points for dE/dx calculation, and their distance of closest approach to the primary vertex (DCA) less than 1 cm. Electrons and positrons are identified using dE/dx in TPC, the velocity (β) calculated from the path length and time of flight between the collision vertex and TOF, and the ratio between the track momentum and energy deposition in the BEMC (pc/E)[38]. The normalized dE/dx is quantified as

$$\mathrm{n}\sigma_e = \frac{\ln(dE/dx)_{\mathrm{measured}} - \ln(dE/dx)^e_{\mathrm{theory}}}{\sigma(\ln(dE/dx))}, \qquad (3)$$

where $(dE/dx)_{\mathrm{measured}}$ is the measured energy loss in the TPC, $(dE/dx)^e_{\mathrm{theory}}$ is the expected energy loss for an electron based on the Bichsel formalism [39], and $\sigma(\ln(dE/dx))$ is the resolution of the $\ln(dE/dx)$ measurement. The value of $\mathrm{n}\sigma_e$ is required to be within $(-1.9, 3)$. A cut of $|1/\beta - 1| < 0.03$ is applied for TOF-associated candidates, and $0.3 < pc/E < 1.5$ is applied for BEMC-associated candidates above 1 GeV/c. The electron and positron candidates are required to pass the $\mathrm{n}\sigma_e$ cut, and either the β or pc/E cut. For HT-triggered events, at least one daughter of a J/ψ candidate must pass the pc/E requirement and have an energy deposition in the BEMC higher than the HT trigger threshold.

B. Analysis procedure

A maximum likelihood method is used to extract all three J/ψ polarization parameters simultaneously. The likelihood is defined as

$$\begin{aligned} &-\ln L(\lambda_\theta, \lambda_\phi, \lambda_{\theta\phi}) \\ &= -\sum N_{J/\psi}(\cos\theta, \phi) \ln[F(\cos\theta, \phi|\lambda_\theta, \lambda_\phi, \lambda_{\theta\phi}) \\ &\quad \times A \times \varepsilon(\cos\theta, \phi)], \end{aligned} \qquad (4)$$

where the sum is taken over the $(\cos\theta, \phi)$ bins, $N_{J/\psi}(\cos\theta, \phi)$ is the raw number of J/ψ candidates in each ($\cos\theta$, ϕ) bin, and $A \times \varepsilon(\cos\theta, \phi)$ is the detector acceptance times J/ψ reconstruction efficiency in the same bin. $F(\cos\theta, \phi|\lambda_\theta, \lambda_\phi, \lambda_{\theta\phi})$ is the integral probability corresponding to $\cos\theta$ and ϕ bin of positrons for given (λ_θ, λ_ϕ, $\lambda_{\theta\phi}$) values, described by Eq. (1) normalized to 1. $A \times \varepsilon(\cos\theta, \phi)$ is evaluated by simulating $J/\psi \to e^+e^-$ decays, passing them through GEANT3 simulation [40] of the STAR detector, embedding the simulated digital signals into real data, and finally reconstructing the embedded events through the same procedure as for the real data. The central values and statistical errors of the J/ψ polarization parameters are obtained by maximizing the likelihood and corrected for possible biases that are estimated from a toy Monte Carlo (ToyMC). In this ToyMC, the same numbers of J/ψ signal and background candidates as in real data are randomly generated with fixed values of polarization parameters after applying detector acceptance and reconstruction efficiencies. The extracted J/ψ polarization parameters from the pseudodata following the same procedure as described above are compared to the input values in terms of both central values and statistical errors, and the differences are applied as corrections to real data, which are generally very small compared to statistical errors.

C. Signal extraction

Invariant mass spectra of electron-positron pairs are shown in Fig. 1 for five different $P_{\mathrm{T}}^{J/\psi}$ bins. The combinatorial background contribution is estimated by summing up the same-sign charge pairs of electron candidates (e^-e^-) and those of positron candidates (e^+e^+), shown as filled areas in the figure. The raw numbers of J/ψ candidates are estimated by subtracting same-sign distributions from opposite-sign ones and integrating resulting counts within the invariant mass window of 3–3.15 GeV/c^2. The contribution from the residual background is found to be between 1.5% and 2.5% and is thus neglected here. The normalized two-dimensional $N_{J/\psi}(\cos\theta, \phi)/N^{\mathrm{total}}_{J/\psi}$ distributions in the HX and CS frames are shown in Fig. 2. The J/ψ reconstruction efficiency multiplied by the detector acceptance, $A \times \varepsilon(\cos\theta, \phi)$, are shown in Fig. 3, corresponding to the invariant mass window of 3–3.15 GeV/c^2. The detector acceptance, track reconstruction, BEMC electron identification, and HT trigger efficiencies are estimated from simulation. Polarization of input J/ψ's does not play any role due to two-dimensional determination of the efficiencies. The electron identification efficiencies due to application of TPC and TOF requirements are estimated from data [23] using a pure electron sample from gamma conversions. The electron dE/dx and $1/\beta$ distributions are fit with a Gaussian distribution to calculate the cut efficiencies. The TOF matching efficiency is evaluated using TPC tracks that are matched to BEMC hits in order to suppress the pileup contribution. The bias due to the geometrical correlation between BEMC and TOF acceptance is corrected using an electron sample from data.

To check the results obtained from fit, the uncorrected J/ψ distributions are compared to the expected ones as shown in Figs. 4 and 5. The former are obtained by projecting two-dimensional $N_{J/\psi}(\cos\theta, \phi)$ distributions onto either the $\cos\theta$ or ϕ direction, while the latter are generated using the extracted J/ψ polarization parameters

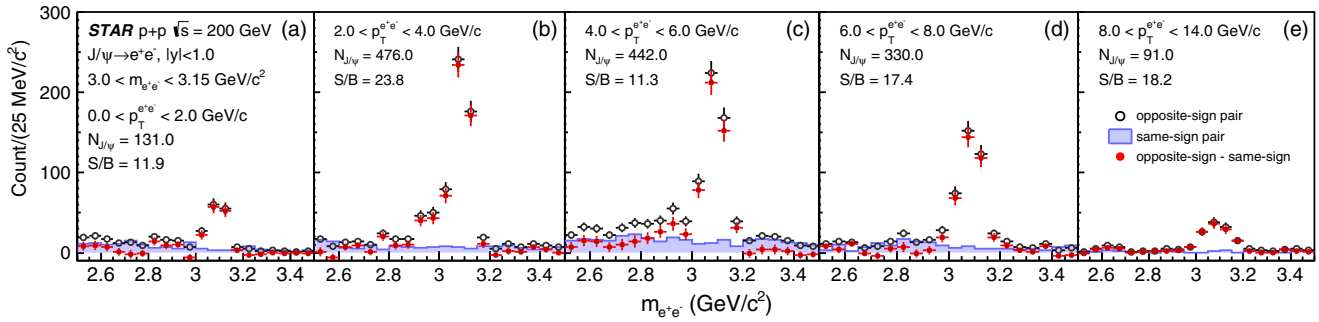

FIG. 1. Invariant mass spectra of electron-positron pairs in different p_{T} bins (from left to right: $p_{\mathrm{T}} = 0$–2, 2–4, 4–6, 6–8, 8–14 GeV$/c$). The black markers (blue filled histograms) are the spectra from opposite-sign (same-sign) charge pairs, while the red markers represent those obtained by subtracting the same-sign spectra from the opposite-sign ones. The number of J/ψ candidates ($N_{J/\psi}$) is given by the number of opposite-sign charge pairs minus that of same-sign charge pairs within $3.0 < m_{e^+e^-} < 3.15$ GeV$/c^2$. The S/B ratio is the ratio between $N_{J/\psi}$ and that of the same-sign charge pairs within $3.0 < m_{e^+e^-} < 3.15$ GeV$/c^2$.

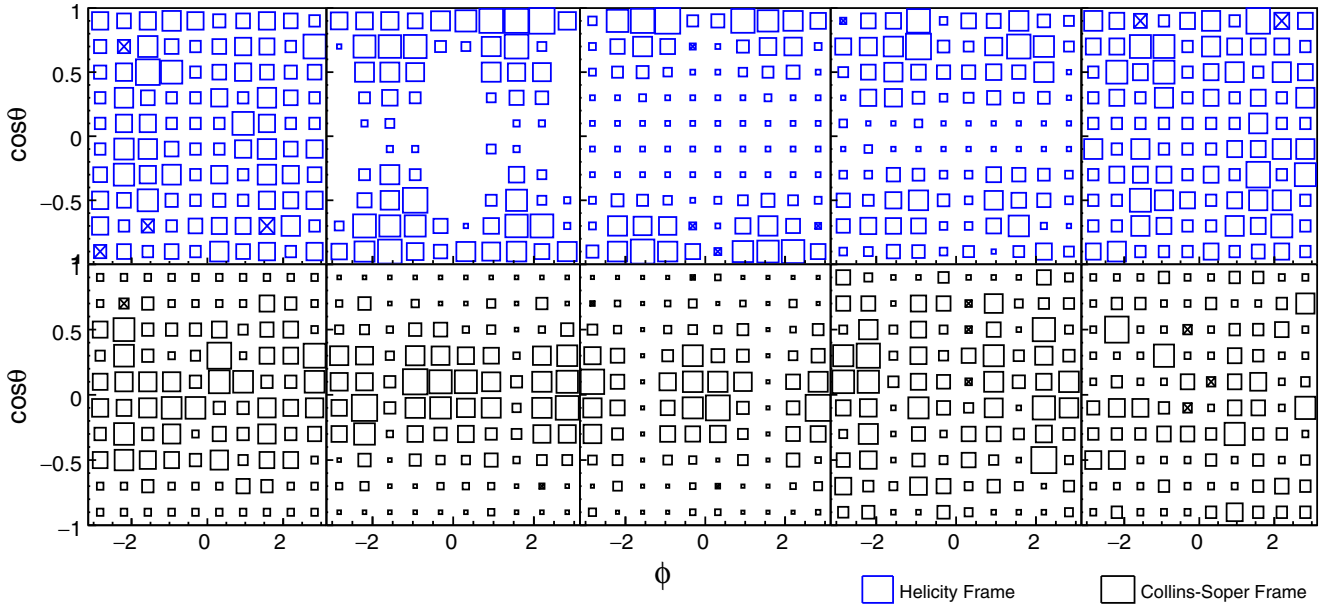

FIG. 2. Normalized two-dimensional $N_{J/\psi}(\cos\theta, \phi)/N_{J/\psi}^{\mathrm{total}}$ distributions in different p_{T} bins (from left to right: $p_{\mathrm{T}} = 0$–2, 2–4, 4–6, 6–8, 8–14 GeV$/c$). The top (bottom) row shows the distributions in the HX (CS) frame. The size of the boxes represents the absolute value of the J/ψ yield. The boxes with crosses are entries with negative values.

from data and taking into account the detector acceptance and efficiency. The expected J/ψ distributions agree well with the measured ones, confirming that the maximum likelihood method can be used to reliably extract the J/ψ polarization parameters. Also shown in these figures as references are the expected $\cos\theta$ and ϕ distributions corresponding to the extreme cases where the polarization parameters $(\lambda_\theta, \lambda_\phi, \lambda_{\theta\phi}) = (\pm 1, 0, 0)$ and $(\lambda_\theta, \lambda_\phi, \lambda_{\theta\phi}) = (0, \pm 1, 0)$ are used, respectively.

The systematic uncertainties are estimated for the following sources:

(1) Acceptance: in extracting efficiencies from simulation, different parameterizations of the inclusive J/ψ p_{T} and rapidity spectra [23] are tried, and the difference is used as the uncertainty.

(2) PID: the uncertainty in the electron identification efficiencies is assessed by varying the mean and width of the TPC $n\sigma_e$ and TOF $1/\beta$ distributions according to their uncertainties in the efficiency calculation and by simultaneously varying the cut in both data and simulation on the ratio between the track momentum and energy deposition in the BEMC from $0.3 < pc/E < 1.5$ to $0.2 < pc/E < 1.4$ or $0.4 < pc/E < 1.6$. Additional uncertainties are considered in evaluating the TOF matching efficiency, including a correction factor to account for the

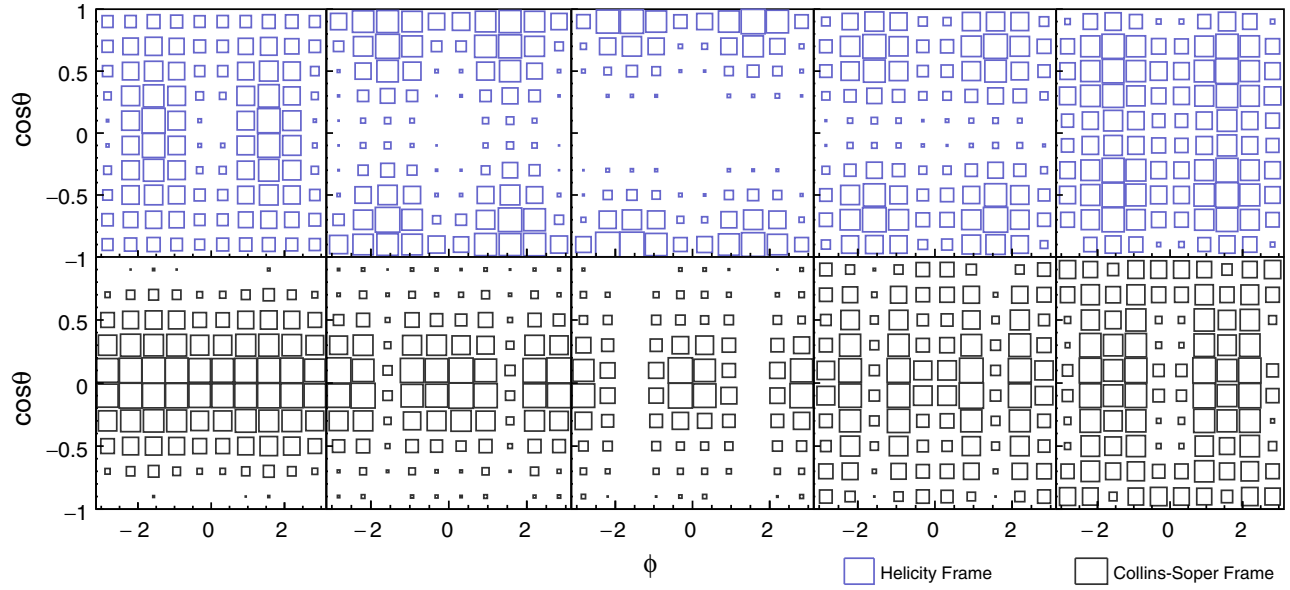

FIG. 3. Two-dimensional $A \times \varepsilon(\cos\theta, \phi)$ distributions in different p_{T} bins (from left to right: $p_{\mathrm{T}} = 0$–2, 2–4, 4–6, 6–8, 8–14 GeV/c). The top (bottom) row shows the distributions in the HX (CS) frame. The size of the boxes represents the value of the J/ψ reconstruction efficiency times acceptance.

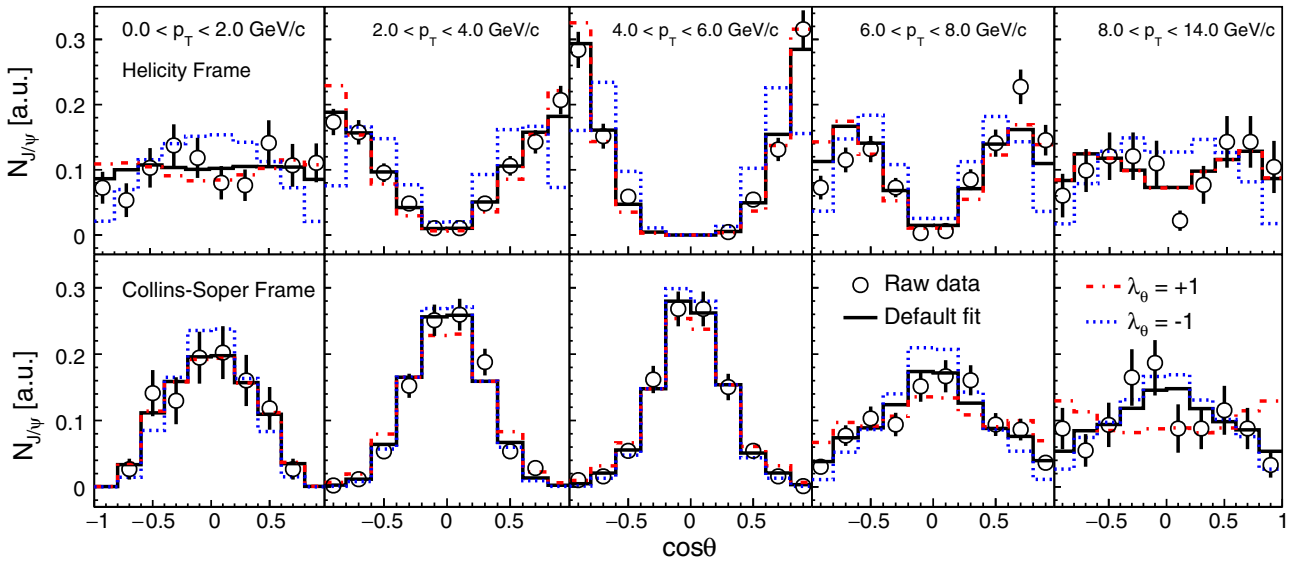

FIG. 4. The number of J/ψ candidates as a function of $\cos\theta$ in different p_{T} bins (from left to right: $p_{\mathrm{T}} = 0$–2, 2–4, 4–6, 6–8, 8–14 GeV/c). The top (bottom) row shows the distributions in the HX (CS) frame. The solid lines correspond to the expected distributions based on the J/ψ polarization parameter values extracted from data. The dashed lines are the expected distributions with assumed values of $(\lambda_\theta, \lambda_\phi, \lambda_{\theta\phi}) = (\pm 1, 0, 0)$. The counts are after arbitrary normalization.

correlation between BEMC and TOF acceptances in obtaining the TOF matching efficiency from data.

(3) Tracking: the uncertainty in track reconstruction efficiency is obtained by simultaneously varying the cuts in data and simulation on the minimum number of TPC hit points from 20 to 18, 19, 22, or 25, on maximum DCA from 1 cm to 0.8 or 1.2 cm, and by varying the momentum resolution in simulation within its uncertainty.

(4) Triggering: the uncertainty in the HT trigger efficiency is obtained by simultaneously changing the HT trigger threshold cut with ±5% variation.

For each of the systematic sources, the same analysis procedure is followed, and the resulting maximum

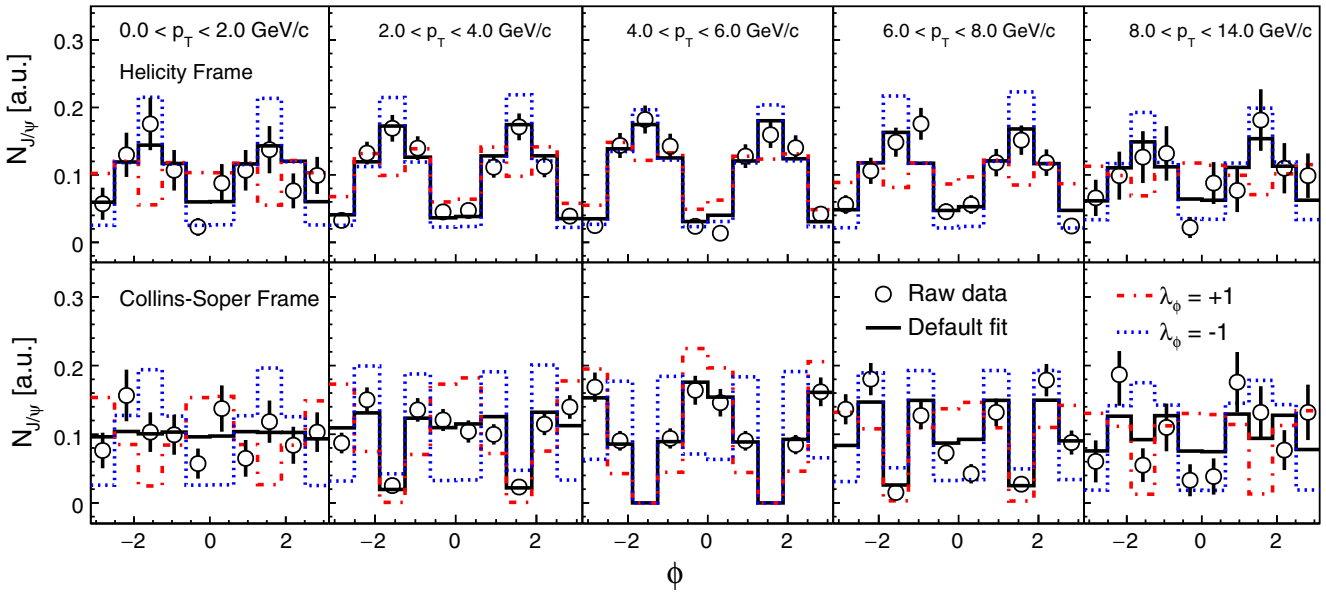

FIG. 5. The number of J/ψ candidates as a function of ϕ in different p_{T} bins (from left to right: $p_{\mathrm{T}} = 0$–2, 2–4, 4–6, 6–8, 8–14 GeV/c). The top (bottom) row shows the distributions in the HX (CS) frame. The solid lines correspond to the expected distributions based on the J/ψ polarization parameter values extracted from data. The dashed lines are the expected distributions with assumed values of $(\lambda_\theta, \lambda_\phi, \lambda_{\theta\phi}) = (0, \pm 1, 0)$. The counts are after arbitrary normalization.

differences to the default results are taken as the uncertainties. The total systematic uncertainties are a quadrature sum of individual sources, as shown in Table I.

IV. $J/\psi \to \mu^+\mu^-$

A. Dataset, event, and track selections

The dataset was taken for $p + p$ collisions at $\sqrt{s} =$ 200 GeV in 2015 and corresponds to an integrated luminosity of 122 pb^{-1}. Events are selected online with a dimuon trigger, which requires at least two signals in the MTD whose timing difference to the start time provided by the VPD falls within the predefined trigger timing window.

Events used in offline analysis are required to have a vertex position of $|V_z^{\mathrm{TPC}}| < 100$ cm along the beam direction to maximize statistics. Primary vertices are further required to be within 2 cm radially with respect to the center of the beam pipe.

In the analysis of the dimuon decay channel, charged tracks reconstructed in the TPC should have at least 15 TPC space points used for reconstruction. The ratio of the number of TPC space points actually used to the maximum possible number of TPC space points is required to be larger than 0.52 to reject split tracks. The DCA to the primary vertex needs to be less than 3 cm to suppress contribution from secondary decays and pileup tracks. The selected TPC tracks are afterward refit with the primary vertex included in order to improve the momentum resolution. Tracks are then propagated from the TPC to the MTD radius. Only tracks with $p_{\mathrm{T}} > 1.3$ GeV/c are selected to achieve high efficiency for reaching the MTD

TABLE I. Summary of systematic uncertainties for $J/\psi \to e^+e^-$ measurement.

Source	p_{T} (GeV/c)	λ_θ^{HX}	λ_ϕ^{HX}	$\lambda_{\theta\phi}^{HX}$	λ_θ^{CS}	λ_ϕ^{CS}	$\lambda_{\theta\phi}^{CS}$
Acceptance	0–2	0.04	0.01	0.04	0.02	0.00	0.00
	2–4	0.01	0.01	0.00	0.15	0.01	0.02
	4–6	0.02	0.01	0.00	0.02	0.01	0.01
	6–8	0.01	0.01	0.00	0.02	0.01	0.00
	8–14	0.03	0.01	0.00	0.01	0.00	0.00
PID	0–2	0.13	0.05	0.10	0.23	0.05	0.05
	2–4	0.12	0.06	0.02	0.03	0.07	0.01
	4–6	0.22	0.10	0.01	0.11	0.11	0.03
	6–8	0.16	0.05	0.05	0.08	0.09	0.03
	8–14	0.11	0.06	0.19	0.03	0.06	0.10
Tracking	0–2	0.13	0.08	0.07	0.39	0.06	0.11
	2–4	0.06	0.05	0.04	0.15	0.04	0.04
	4–6	0.08	0.09	0.05	0.14	0.04	0.04
	6–8	0.24	0.04	0.05	0.12	0.15	0.04
	8–14	0.33	0.05	0.12	0.06	0.10	0.11
Trigger	0–2	0.00	0.00	0.00	0.00	0.00	0.00
	2–4	0.04	0.03	0.01	0.01	0.02	0.02
	4–6	0.17	0.17	0.01	0.14	0.02	0.10
	6–8	0.10	0.03	0.03	0.06	0.03	0.03
	8–14	0.12	0.00	0.01	0.01	0.03	0.00
Total	0–2	0.19	0.10	0.12	0.45	0.08	0.12
	2–4	0.14	0.09	0.05	0.21	0.08	0.05
	4–6	0.29	0.22	0.05	0.22	0.12	0.11
	6–8	0.30	0.07	0.07	0.15	0.18	0.06
	8–14	0.37	0.08	0.22	0.07	0.12	0.15

after losing energy along the trajectory. Once a track is matched to the closest MTD hit, cuts on variables, Δy, Δz and $\Delta t_{\rm tof}$, are applied to further suppress background hadrons. Here, Δy and Δz are the residuals between the projected track position at the MTD radius and the matched MTD hit along azimuthal and beam directions, respectively. We require Δy and Δz to be within 3 (3.5) σ of their resolutions for $p_{\rm T} < (>)3$ GeV/c. $\Delta t_{\rm tof}$ is the difference between the measured time of flight with the MTD and the calculated time of flight from track extrapolation with a muon particle hypothesis and should satisfy $|\Delta t_{\rm tof}| < 1$ ns. Additional PID capabilities arise from the energy loss measurement in the TPC. It is quantified as $n\sigma_\pi$, whose definition is similar to that of electrons as described in Sec. III A but using a pion hypothesis. In the kinematic range relevant for this analysis, muons are expected to lose more energy than pions by about half of dE/dx resolution. A cut of $-2 < n\sigma_\pi < 3$ is applied.

B. Analysis procedure

To extract the J/ψ polarization in the dimuon decay channel, a different strategy is adopted compared to the one used for the dielectron channel as described in Sec. III B. Equation (1) is integrated over ϕ and $\cos\theta$, yielding two one-dimensional (1D) distributions:

$$W(\cos\theta) \propto 1 + \lambda_\theta \cos^2\theta, \tag{5}$$

and

$$W(\phi) \propto 1 + \frac{2\lambda_\phi}{3+\lambda_\theta}\cos 2\phi, \tag{6}$$

The $\lambda_{\theta\phi}$ term vanishes in both integrations. The polarization parameters, λ_θ and λ_ϕ, are extracted from a simultaneous fit to corrected J/ψ yield distributions as a function of $\cos\theta$ and ϕ of daughter μ^+ with Eqs. (5) and (6). This strategy is motivated by the worse signal-to-background ratio for the dimuon decay channel compared to the dielectron decay channel, and fitting the 1D distributions of Eqs. (5) and (6) is therefore more stable. However, the $\lambda_{\theta\phi}$ parameter cannot be extracted from this method.

The number of J/ψ extracted in each $\cos\theta$ or ϕ bin needs to be corrected for the detector acceptance and efficiency, denoted as $A \times \varepsilon(\cos\theta, \phi)$. It is evaluated via simulation as described in Sec. III B but for the muon channel. Since $A \times \varepsilon(\cos\theta, \phi)$ depends on both $\cos\theta$ and ϕ, the projected 1D $A \times \varepsilon$ as a function of $\cos\theta$ or ϕ is affected by the assumed polarization of input J/ψ in the simulation. On the other hand, the $\lambda_{\theta\phi}$ value does not affect the averaged $A \times \varepsilon$ as $A \times \varepsilon(\cos\theta, \phi)$ is symmetric with respect to $\cos\theta = 0$ and $|\phi - \pi/2| = 0$. Given that the J/ψ polarization is not known *a priori* and the correction for the detector acceptance and efficiency depends on it, an iterative procedure is adopted. In the first iteration, the 1D $A \times \varepsilon$ as a function of $\cos\theta$ or ϕ is evaluated using nonpolarized J/ψ in the simulation, and the polarization parameters are extracted from data after correcting for $A \times \varepsilon$. In the second iteration, the extracted polarization parameters from the previous iteration are used in the simulation to assess $A \times \varepsilon$, which in turn is used to correct data and obtain new polarization parameters. The iteration continues until the differences of the obtained polarization parameters between two consecutive iterations are less than 0.01. This threshold is determined based on the statistical precision of the data.

To validate the iterative procedure, a ToyMC is developed which is different from that used in the electron channel analysis. The single muon efficiency as a function of $p_{\rm T}$, η, and ϕ, extracted from the GEANT simulations, is applied to mimic realistic detector acceptance and detection efficiency. J/ψ's with realistic λ_θ and λ_ϕ values in four different $p_{\rm T}$ bins, as presented in Sec. V, are used as input to the ToyMC, while the $\lambda_{\theta\phi}$ value is assumed to be 0. Both pseudodata and J/ψ pseudoefficiency are generated in the ToyMC. Depending on the statistical precision of the pseudodata and how the pseudoefficiency is obtained, the following tests are done:

(i) Test 1.—Large statistics with correct efficiency ("Large stat., corr. eff."): the pseudodata sample has significantly larger statistics than real data, and the pseudoefficiency is generated using the same polarization parameters as for pseudodata. This represents a best-case scenario, and the polarization parameters, λ_θ, λ_ϕ, and $\lambda_{\rm inv}$, are extracted using Eqs. (5) and (6). Differences to the input polarization values are shown in Fig. 6 as open circles for both HX and CS frames. In most cases, the input values are recovered with small discrepancies arising from the limited acceptance of the MTD.

(ii) Test 2.—Limited statistics with correct efficiency ("Limited stat., corr. eff."): the pseudodata sample has comparable statistical precision to real data, while the pseudoefficiency is generated using the

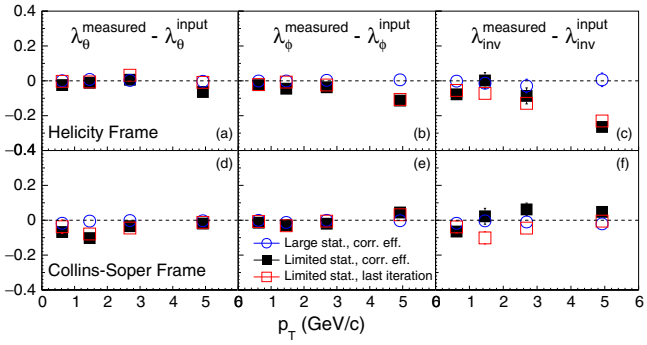

FIG. 6. Differences of the extracted J/ψ polarization parameters, λ_θ, λ_ϕ and $\lambda_{\rm inv}$, in the ToyMC and the input values in both the HX and CS frames. Data points of different markers correspond to the three different tests. See the text for details.

same polarization parameters as for pseudodata. To avoid random fluctuation of one pseudodata sample, 500 independent samples of similar statistics are generated. The mean values of the polarization parameters extracted from the 500 pseudodata samples are compared to the input values, and the differences are shown in Fig. 6 as filled squares. Compared to "Test 1," the extracted polarization values deviate further from the input ones due to the influence of the limited statistics in the pseudodata sample on top of the limited MTD acceptance. The relatively large deviation seen in λ_{inv} around 5 GeV/c in the HX frame is an amplification of the smaller, but still sizable, deviation seen in λ_ϕ.

(iii) Test 3.—Limited statistics using the iterative procedure ("Limited stat., last iteration"): in the last test, the 500 pseudodata samples are generated with comparable statistical precision to real data, but the iterative procedure as described above is used to obtain the efficiency. Polarization values equal to 0 are used in the first iteration, and the procedure stops after the same convergence criterion of 0.01, as for the real data, between two consecutive iterations is fulfilled. The resulting differences to the input values are shown as open squares in Fig. 6 and agree with "Test 2" quite well. This indicates that very small biases are introduced in the iterative procedure.

It has also been found that the correct polarization values are always obtained as long as the convergence occurs and no matter what input polarization values are used in the first iteration. The ToyMC validation confirms that the J/ψ polarization parameters can be extracted reliably using the iterative procedure. The residual biases shown in Fig. 6 are corrected for, as described in Sec. IV C.

C. Signal extraction

The selected muon candidates of opposite-sign charges are paired, and the resulting invariant mass distribution is shown in Fig. 7 for the entire sample used in the dimuon channel analysis. The raw J/ψ yield is extracted by fitting the invariant mass distribution with a Gaussian function describing the J/ψ signal and a polynomial function describing the background. Data points in the $\psi(2S)$ mass region ($3.6 < M_{\mu\mu} < 3.8$ GeV/c^2) are excluded from the fit. The mean of the Gaussian distribution is fixed to the J/ψ mass in the PDG [41]. In total, the J/ψ yields are extracted in 10 $\cos\theta$ bins and 15 ϕ bins for each $p_{\text{T}}^{J/\psi}$ interval. The order of the background polynomial function ranges from 2 to 5, depending on the $p_{\text{T}}^{J/\psi}$ and the μ^+ $\cos\theta$ and ϕ bin. To facilitate the fits below 2 GeV/c, the widths of the Gaussian function in individual $\cos\theta$ and ϕ bins are fixed to be the same as that extracted from fitting the inclusive invariant mass distribution integrated over $\cos\theta$

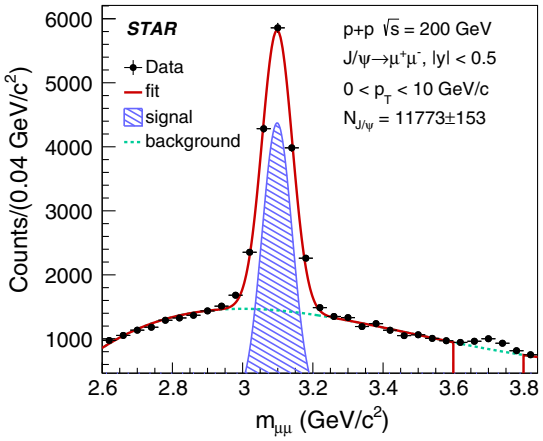

FIG. 7. The invariant mass spectrum of opposite-sign muon pairs for $p_{\text{T}} < 10$ GeV/c. The solid line depicts the fitting result, consisting of a Gaussian function representing the signal (shaded area) and a polynomial function describing the background (dashed line). Data points in the $\psi(2S)$ mass region ($3.6 < M_{\mu\mu} < 3.8$ GeV/c^2) are excluded from the fit.

and ϕ bins in the same $p_{\text{T}}^{J/\psi}$ interval. For $p_{\text{T}}^{J/\psi}$ above 2 GeV/c, the width of the Gaussian function is left as a free parameter. Variations in the following aspects of the fit procedure are applied: the bin width of the invariant mass distribution, fixing the width of the Gaussian function also for $p_{\text{T}}^{J/\psi}$ above 2 GeV/c, the order of the polynomial function, and the fit range. The average J/ψ yields from these variations are used for extracting the polarization parameters. J/ψ yields with significance less than 3 are not considered. Upper panels of Fig. 8 show an example of the average raw J/ψ yield, depicted as open circles, as a function of $\cos\theta$ and ϕ for $0 < p_{\text{T}}^{J/\psi} < 1$ GeV/c in the HX frame.

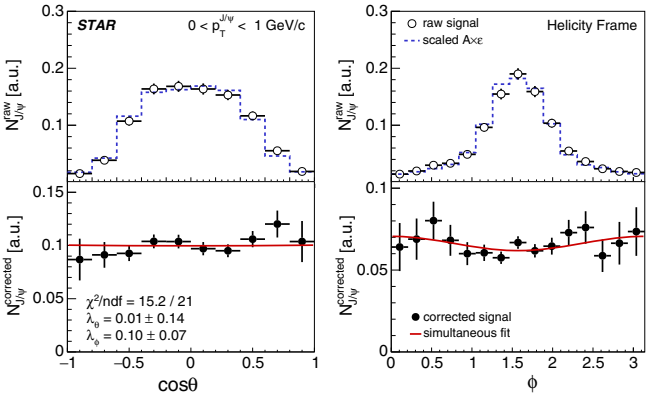

FIG. 8. Upper: the raw J/ψ yield and $A \times \varepsilon$ from the last iteration as a function of μ^+ $\cos\theta$ (left) and ϕ (right) in the HX frame for $0 < p_{\text{T}}^{J/\psi} < 1$ GeV/c. Lower: the acceptance and efficiency corrected J/ψ yields along with the simultaneous fit. The counts are after arbitrary normalization.

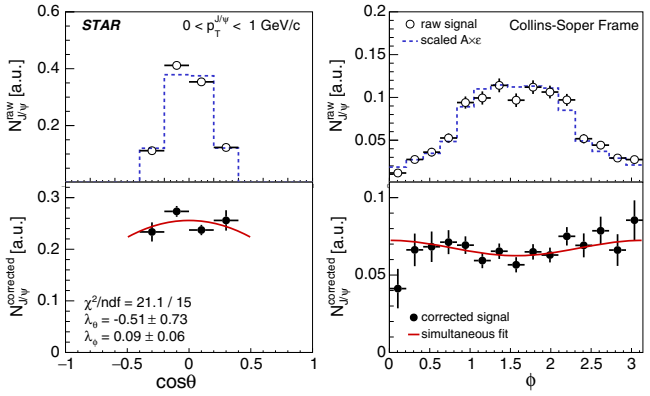

FIG. 9. Upper: the raw J/ψ yield and $A \times \varepsilon$ from the last iteration as a function of μ^+ $\cos\theta$ (left) and ϕ (right) in the CS frame for $0 < p_{\mathrm{T}}^{J/\psi} < 1$ GeV/c. Lower: the acceptance and efficiency corrected J/ψ yields along with the simultaneous fit. The counts are after arbitrary normalization.

Following the iterative procedure, the efficiency multiplied by the detector acceptance from the last iteration is shown in the upper panel of Fig. 8 as dashed lines. It is scaled to the same integral as the data distribution. The lower panels of Fig. 8 show the fully corrected J/ψ yield as a function of $\cos\theta$ and ϕ, along with the simultaneous fit to both distributions using Eqs. (5) and (6) (solid lines). The polarization parameters, λ_θ and λ_ϕ, are obtained from the simultaneous fit and listed in the figure. Similar plots in the CS frame are shown in Fig. 9 for $0 < p_{\mathrm{T}}^{J/\psi} < 1$ GeV/c. The average λ_θ and λ_ϕ values from 24 combinations of different track quality and muon identification cuts are taken as the central values. Figures 8 and 9 show results from one such combination as an example. As shown in Fig. 6, small biases are present in the extracted polarization parameters, due to a combination of limited MTD acceptance, limited statistical precision of data, and the usage of the iterative procedure. Using the ToyMC described above, the extracted J/ψ polarization parameters are compared with input values in terms of central values and statistical errors, and the differences are applied as corrections to real data, which are also very small compared to statistical errors.

The systematic uncertainties arise from signal extraction, detector acceptance, and efficiency. As mentioned above, different aspects of the fitting procedure are varied, and 24 combinations of track quality and muon identification cuts are tried. For the latter, cuts are changed consistently in data and MC simulation, and the entire analysis chain is repeated for each case. The root mean squares of the distributions for polarization parameters stemming from these two groups of variations are taken as the systematic uncertainties. The total systematic uncertainties are a quadrature sum of individual sources, as shown in Table II.

TABLE II. Summary of systematic uncertainties for $J/\psi \to \mu^+\mu^-$ measurement.

Source	p_{T} (GeV/c)	λ_θ^{HX}	λ_ϕ^{HX}	λ_θ^{CS}	λ_ϕ^{CS}
Signal extraction	0–1	0.10	0.02	0.19	0.03
	1–2	0.29	0.05	0.31	0.09
	2–4	0.05	0.03	0.09	0.06
	4–10	0.15	0.05	0.09	0.20
Tracking and PID	0–1	0.04	0.02	0.24	0.02
	1–2	0.11	0.07	0.33	0.07
	2–4	0.10	0.10	0.12	0.08
	4–10	0.06	0.05	0.12	0.08
Total	0–1	0.11	0.03	0.32	0.04
	1–2	0.31	0.09	0.45	0.11
	2–4	0.11	0.10	0.16	0.10
	4–10	0.17	0.07	0.15	0.22

V. RESULTS

The polarization parameters, λ_θ, λ_ϕ and $\lambda_{\theta\phi}$ for inclusive J/ψ are measured in both the HX and CS frames in $p + p$ collisions at $\sqrt{s} = 200$ GeV/c, as shown in Fig. 10. The dimuon and dielectron results are shown as filled and open symbols, respectively, and are consistent with each other in

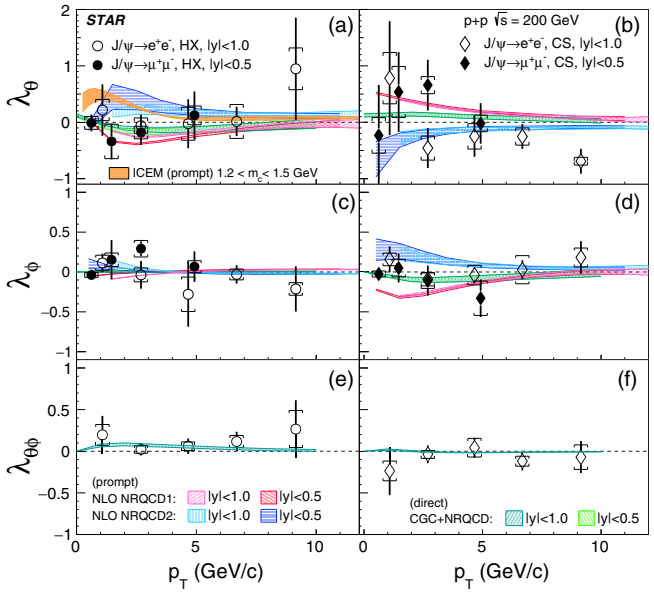

FIG. 10. The J/ψ polarization parameters (from top to bottom: λ_θ, λ_ϕ, $\lambda_{\theta\phi}$) as a function of p_{T} in the HX (left) and CS (right) frames. Open and filled symbols are for measurements through the dielectron and dimuon decay channels covering different rapidity ranges. The vertical bars represent the statistical errors, while the boxes around data points depict the systematic uncertainties. The data points are placed at the mean p_{T} value determined from the inclusive $p_{\mathrm{T}}^{J/\psi}$ spectrum measured in $p + p$ collisions at $\sqrt{s} = 200$ GeV [23]. Model calculations [8,14,20,42] are also shown for comparison. The ICEM and two NLO NRQCD calculations are for prompt J/ψ, while the CGC + NRQCD is for direct J/ψ.

TABLE III. List of χ^2/NDF and the corresponding p-values between data of inclusive J/ψ polarization and different model calculations of prompt or direct J/ψ polarization.

Model	χ^2/NDF	p-value
ICEM [8]	13.28/9	0.150
NRQCD1 [42]	48.81/32	0.029
NRQCD2 [14]	42.99/32	0.093
CGC + NRQCD [20]	32.11/46	0.940

the overlapping p_T range even though they cover different rapidity regions. Measurements of $\lambda_{\theta\phi}$ via the dimuon channel, currently not available, will be carried out in the future with a larger data sample than the one used in this paper. All three polarization parameters are consistent with 0 within statistical and systematic uncertainties, except for λ_θ in the CS frame above 8 GeV/c whose central value is at $-0.69 \pm 0.22 \pm 0.07$. No strong p_T dependence is seen in all cases. The numerical values of the measured J/ψ polarization parameters are listed in the Appendix (Tables IV,V,VI,VII). Model calculations for prompt J/ψ from ICEM [8], NRQCD with two sets of LDMEs denoted as "NLO NRQCD1" [42] and "NLO NRQCD2" [14], are shown in Fig. 10 for comparison. Nonprompt J/ψ from b hadron decays, not included in aforementioned model calculations, make about 10%–25% of the inclusive J/ψ sample above 5 GeV/c, with the fraction decreasing to be negligible at 1 GeV/c [13]. The effective polarization for nonprompt J/ψ above 5 GeV/c within $|y| < 0.6$ is measured to be $\lambda_\theta = -0.106 \pm 0.033 \pm 0.007$ in $p + \bar{p}$ collisions at $\sqrt{s} = 1.96$ TeV [43]. Therefore, contribution to the inclusive J/ψ polarization from b hadron decays is expected to be small. Also shown in Fig. 10 are CGC + NRQCD calculations for direct J/ψ, in which both nonprompt J/ψ and those from decays of excited charmonium states are not included [20]. A recent CMS measurement supports that at least one of χ_{c1} and χ_{c2} is strongly polarized in the HX frame in $p + p$ collisions at 8 TeV, in agreement with NRQCD predictions [44]. It has been checked explicitly in Ref. [19] that feeddown corrections from χ_{cJ} states on J/ψ polarization parameters are small and within theoretical uncertainties. For λ_θ in the HX frame, the ICEM calculation predicts a sizable transverse polarization at low p_T, while the J/ψ polarization from CGC + NRQCD changes from slightly transverse at low p_T to slightly longitudinal at higher p_T. The difference between the LDMEs used in the two NLO NRQCD calculations is that additional η_c production data measured by the LHCb Collaboration [15] are used to determine LDMEs for "NLO NRQCD1" besides those used for the case of "NLO NRQCD2." They show opposite behaviors for λ_θ and λ_ϕ in both reference frames. To quantify the agreement between data and model calculations, the χ^2 test has been performed simultaneously using the data points in HX and CS frames for both channels. The χ^2/NDF and corresponding p-values are listed in Table III.

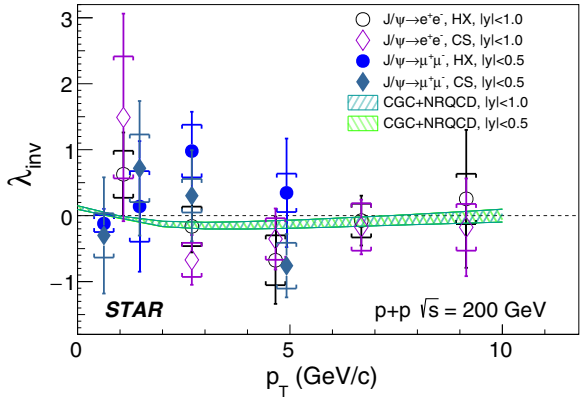

FIG. 11. λ_{inv} of J/ψ vs p_T in both HX (circles) and CS (diamonds) reference frames. The open and filled symbols are for measurements through the dielectron and dimuon decay channels, respectively. The vertical bars represent the statistical errors, while the boxes around data points depict the systematic uncertainties. CGC + NRQCD [20] calculations are also shown for comparison.

While no model can be ruled out definitively based solely on the data presented, the CGC + NRQCD gives the best overall description.

The λ_{inv} values extracted according to Eq. (2) for inclusive J/ψ are shown in Fig. 11 as a function of p_T for both the HX and CS frames. The dimuon and dielectron results are shown as filled and open circles, respectively. The vertical bars represent the statistical errors, while the boxes around data points depict the systematic uncertainties. The λ_{inv} values measured in the two frames are consistent with each other within experimental uncertainties, confirming the reliability of the results. The λ_{inv} values are consistent with the CGC + NRQCD calculations within uncertainties.

VI. SUMMARY

For the first time, the inclusive J/ψ polarization parameters, λ_θ, λ_ϕ and $\lambda_{\theta\phi}$, are measured as a function of p_T in $p + p$ collisions at $\sqrt{s} = 200$ GeV in both the helicity and Collins-Soper reference frames. Results utilizing the dimuon and dielectron decay channels are presented and agree with each other within uncertainties although slightly different kinematic ranges are covered. The inclusive J/ψ's do not exhibit significant transverse or longitudinal polarization with little dependence on p_T. Among several model calculations compared to data, the CGC + NRQCD agrees the best overall. These results provide additional tests and valuable guidance for theoretical efforts toward a complete understanding of the J/ψ production mechanism in vacuum.

ACKNOWLEDGMENTS

We thank the RHIC Operations Group and RCF at BNL, the NERSC Center at LBNL, and the Open Science Grid consortium for providing resources and support. This work was supported in part by the Office of Nuclear Physics within the U.S. DOE Office of Science; the U.S. National Science Foundation; the Ministry of Education and Science of the Russian Federation; National Natural Science Foundation of China; Chinese Academy of Science; the Ministry of Science and Technology of China and the Chinese Ministry of Education; the Higher Education Sprout Project by Ministry of Education at NCKU; the National Research Foundation of Korea; Czech Science Foundation and Ministry of Education, Youth and Sports of the Czech Republic; Hungarian National Research, Development and Innovation Office; New National Excellency Programme of the Hungarian Ministry of Human Capacities; Department of Atomic Energy and Department of Science and Technology of the Government of India; the National Science Centre of Poland; the Ministry of Science Education and Sports of the Republic of Croatia; RosAtom of Russia and German Bundesministerium fur Bildung, Wissenschaft, Forschung and Technologie (BMBF); Helmholtz Association; Ministry of Education, Culture, Sports, Science, and Technology (MEXT); and Japan Society for the Promotion of Science (JSPS).

APPENDIX: DATA TABLES

The values of inclusive J/ψ polarization parameters in different p_T bins are shown in Tables IV, V, VI, and VII.

TABLE IV. The inclusive J/ψ polarization parameters in the HX frame in different p_T bins measured through the dielectron channel within $|y| < 1$. The first uncertainty is statistical, and the second is systematic.

p_T (GeV/c)	$\langle p_T \rangle$ (GeV/c)	λ_θ^{HX}	λ_ϕ^{HX}	$\lambda_{\theta\phi}^{HX}$	$\lambda_{\text{inv}}^{HX}$
0–2	1.08	$0.22 \pm 0.46 \pm 0.19$	$0.11 \pm 0.12 \pm 0.10$	$0.20 \pm 0.23 \pm 0.12$	$0.63 \pm 0.63 \pm 0.36$
2–4	2.69	$-0.06 \pm 0.19 \pm 0.14$	$-0.04 \pm 0.17 \pm 0.09$	$0.02 \pm 0.07 \pm 0.05$	$-0.16 \pm 0.39 \pm 0.30$
4–6	4.66	$-0.03 \pm 0.43 \pm 0.29$	$-0.28 \pm 0.41 \pm 0.22$	$0.06 \pm 0.09 \pm 0.05$	$-0.68 \pm 0.66 \pm 0.38$
6–8	6.68	$0.01 \pm 0.26 \pm 0.30$	$-0.03 \pm 0.12 \pm 0.07$	$0.12 \pm 0.12 \pm 0.07$	$-0.07 \pm 0.38 \pm 0.26$
8–14	9.15	$0.95 \pm 0.91 \pm 0.37$	$-0.21 \pm 0.28 \pm 0.08$	$0.27 \pm 0.35 \pm 0.22$	$0.25 \pm 1.05 \pm 0.38$

TABLE V. The inclusive J/ψ polarization parameters in the CS frame in different p_T bins measured through the dielectron channel within $|y| < 1$. The first uncertainty is statistical, and the second is systematic.

p_T (GeV/c)	$\langle p_T \rangle$ (GeV/c)	λ_θ^{CS}	λ_ϕ^{CS}	$\lambda_{\theta\phi}^{CS}$	$\lambda_{\text{inv}}^{CS}$
0–2	1.08	$0.78 \pm 1.01 \pm 0.45$	$0.16 \pm 0.16 \pm 0.08$	$-0.24 \pm 0.29 \pm 0.12$	$1.49 \pm 1.57 \pm 0.92$
2–4	2.69	$-0.46 \pm 0.35 \pm 0.21$	$-0.09 \pm 0.08 \pm 0.08$	$-0.04 \pm 0.11 \pm 0.05$	$-0.67 \pm 0.38 \pm 0.26$
4–6	4.66	$-0.25 \pm 0.36 \pm 0.22$	$-0.04 \pm 0.10 \pm 0.12$	$0.04 \pm 0.12 \pm 0.11$	$-0.35 \pm 0.46 \pm 0.32$
6–8	6.68	$-0.25 \pm 0.22 \pm 0.15$	$0.03 \pm 0.12 \pm 0.18$	$-0.12 \pm 0.11 \pm 0.06$	$-0.17 \pm 0.41 \pm 0.36$
8–14	9.15	$-0.69 \pm 0.22 \pm 0.07$	$0.18 \pm 0.20 \pm 0.12$	$-0.07 \pm 0.19 \pm 0.15$	$-0.18 \pm 0.74 \pm 0.35$

TABLE VI. The inclusive J/ψ polarization parameters in the HX frame in different p_T bins measured through the dimuon channel within $|y| < 0.5$. The first uncertainty is statistical, and the second is systematic.

p_T (GeV/c)	$\langle p_T \rangle$ (GeV/c)	λ_θ^{HX}	λ_ϕ^{HX}	$\lambda_{\text{inv}}^{HX}$
0–1	0.62	$-0.01 \pm 0.15 \pm 0.11$	$-0.04 \pm 0.06 \pm 0.03$	$-0.12 \pm 0.22 \pm 0.13$
1–2	1.46	$-0.34 \pm 0.32 \pm 0.31$	$0.15 \pm 0.25 \pm 0.09$	$0.14 \pm 0.99 \pm 0.54$
2–4	2.69	$-0.18 \pm 0.22 \pm 0.11$	$0.29 \pm 0.09 \pm 0.10$	$0.98 \pm 0.60 \pm 0.40$
4–10	4.92	$0.12 \pm 0.42 \pm 0.17$	$-0.07 \pm 0.19 \pm 0.07$	$0.35 \pm 0.82 \pm 0.30$

TABLE VII. The inclusive J/ψ polarization parameters in the CS frame in different p_{T} bins measured through the dimuon channel within $|y| < 0.5$. The first uncertainty is statistical, and the second is systematic.

p_{T} (GeV/c)	$\langle p_{\mathrm{T}} \rangle$ (GeV/c)	λ_θ^{CS}	λ_ϕ^{CS}	$\lambda_{\mathrm{inv}}^{CS}$
0–1	0.62	$-0.23 \pm 0.89 \pm 0.32$	$-0.03 \pm 0.05 \pm 0.04$	$-0.30 \pm 0.88 \pm 0.34$
1–2	1.46	$0.54 \pm 0.71 \pm 0.45$	$0.05 \pm 0.18 \pm 0.11$	$0.72 \pm 1.02 \pm 0.51$
2–4	2.69	$0.66 \pm 0.45 \pm 0.15$	$-0.11 \pm 0.19 \pm 0.10$	$0.30 \pm 0.69 \pm 0.25$
4–10	4.92	$-0.02 \pm 0.36 \pm 0.15$	$-0.33 \pm 0.24 \pm 0.22$	$-0.76 \pm 0.48 \pm 0.35$

[1] J. Adam *et al.* (STAR Collaboration), Measurement of inclusive J/ψ suppression in Au + Au collisions at $\sqrt{s_{NN}} =$ 200 GeV through the dimuon channel at STAR, Phys. Lett. B **797**, 134917 (2019).

[2] J.-P. Lansberg, New observables in inclusive production of quarkonia, arXiv:1903.09185 [Phys. Rep. (to be published)].

[3] H. Fritzsch, Producing heavy quark flavors in hadronic collisions: A test of quantum chromodynamics, Phys. Lett. **67B**, 217 (1977).

[4] F. Halzen, CVC for gluons and hadroproduction of quark flavors, Phys. Lett. **69B**, 105 (1977).

[5] Y.-Q. Ma and R. Vogt, Quarkonium production in an improved color evaporation model, Phys. Rev. D **94**, 114029 (2016).

[6] M. Cacciari, M. Greco, and P. Nason, The p_T spectrum in heavy-flavor hadroproduction, J. High Energy Phys. 05 (1998) 007.

[7] J. Adam *et al.* (STAR Collaboration), Measurements of the transverse-momentum-dependent cross sections of J/ψ production at mid-rapidity in proton + proton collisions at $\sqrt{s} = 510$ and 500 GeV with the STAR detector, Phys. Rev. D **100**, 052009 (2019).

[8] V. Cheung and R. Vogt, Production and polarization of prompt J/ψ in the improved color evaporation model using the k_T-factorization approach, Phys. Rev. D **98**, 114029 (2018).

[9] B. Abelev *et al.* (ALICE Collaboration), J/ψ Polarization in pp Collisions at $\sqrt{s} = 7$ TeV, Phys. Rev. Lett. **108**, 082001 (2012).

[10] R. Aaij *et al.* (LHCb Collaboration), Measurement of J/ψ polarization in pp collisions at $\sqrt{s} = 7$ TeV, Eur. Phys. J. C **73**, 2631 (2013).

[11] G. T. Bodwin, E. Braaten, and G. P. Lepage, Rigorous QCD analysis of inclusive annihilation and production of heavy quarkonium, Phys. Rev. D **51**, 1125 (1995); Erratum, Phys. Rev. D **55**, 5853 (1997).

[12] M. Butenschoen and B. A. Kniehl, J/ψ Polarization at Tevatron and LHC: Nonrelativistic-QCD Factorization at the Crossroads, Phys. Rev. Lett. **108**, 172002 (2012).

[13] K.-T. Chao, Y.-Q. Ma, H.-S. Shao, K. Wang, and Y.-J. Zhang, J/ψ Polarization at Hadron Colliders in Nonrelativistic QCD, Phys. Rev. Lett. **108**, 242004 (2012).

[14] B. Gong, L.-P. Wan, J.-X. Wang, and H.-F. Zhang, Polarization for Prompt J/ψ and $\psi(2S)$ Production at the Tevatron and LHC, Phys. Rev. Lett. **110**, 042002 (2013).

[15] R. Aaij *et al.* (LHCb Collaboration), Measurement of the $\eta_c(1S)$ production cross-section in proton-proton collisions via the decay $\eta_c(1S) \to p\bar{p}$, Eur. Phys. J. C **75**, 311 (2015).

[16] T. Affolder *et al.* (CDF Collaboration), Measurement of J/ψ and $\psi(2S)$ Polarization in $p + \bar{p}$ Collisions at $\sqrt{s} = 1.8$ TeV, Phys. Rev. Lett. **85**, 2886 (2000).

[17] A. Abulencia *et al.* (CDF Collaboration), Polarizations of J/ψ and $\psi(2S)$ Mesons Produced in $p\bar{p}$ Collisions at $\sqrt{s} = 1.96$ TeV, Phys. Rev. Lett. **99**, 132001 (2007).

[18] E. Iancu and R. Venugopalan, *The Color Glass Condensate and High-Energy Scattering in QCD* (World Scientific, Singapore, 2004), p. 249.

[19] Y.-Q. Ma and R. Venugopalan, Comprehensive Description of J/ψ Production in Proton-Proton Collisions at Collider Energies, Phys. Rev. Lett. **113**, 192301 (2014).

[20] Y.-Q. Ma, T. Stebel, and R. Venugopalan, J/ψ polarization in the CGC + NRQCD approach, J. High Energy Phys. 12 (2018) 057.

[21] A. Adare *et al.* (PHENIX Collaboration), Transverse momentum dependence of J/ψ polarization at midrapidity in $p + p$ collisions at $\sqrt{s} = 200$ GeV, Phys. Rev. D **82**, 012001 (2010).

[22] L. Adamczyk *et al.* (STAR Collaboration), J/ψ production at high transverse momenta in $p + p$ and Au + Au collisions at $\sqrt{s_{NN}} = 200$ GeV, Phys. Lett. B **722**, 55 (2013).

[23] J. Adam *et al.* (STAR Collaboration), J/ψ production cross section and its dependence on charged-particle multiplicity in $p + p$ collisions at $\sqrt{s} = 200$ GeV, Phys. Lett. B **786**, 87 (2018).

[24] L. Adamczyk *et al.* (STAR Collaboration), J/ψ polarization in $p + p$ collisions at $\sqrt{s} = 200$ GeV in STAR, Phys. Lett. B **739**, 180 (2014).

[25] M. Noman and S. D. Rindani, Angular distribution of muons pair—Produced in pp collisions, Phys. Rev. D **19**, 207 (1979).

[26] M. Jacob and G. C. Wick, On the general theory of collisions for particles with spin, Ann. Phys. (N.Y.) **7**, 404 (1959); Erratum, Ann. Phys. (Amsterdam) **281**, 774 (2000).

[27] J. C. Collins and D. E. Soper, Angular distribution of dileptons in high-energy hadron collisions, Phys. Rev. D **16**, 2219 (1977).

[28] P. Faccioli, C. Lourenço, J. Seixas, and H. K. Wöhri, Towards the experimental clarification of quarkonium polarization, Eur. Phys. J. C **69**, 657 (2010).

[29] S. Digal, P. Petreczky, and H. Satz, Quarkonium feed down and sequential suppression, Phys. Rev. D **64**, 094015 (2001).
[30] K. H. Ackermann *et al.*, STAR detector overview, Nucl. Instrum. Methods Phys. Res., Sect. A **499**, 624 (2003).
[31] M. Anderson *et al.*, The STAR time projection chamber: A unique tool for studying high multiplicity events at RHIC, Nucl. Instrum. Methods Phys. Res., Sect. A **499**, 659 (2003).
[32] F. Bergsma *et al.*, The STAR detector magnet subsystem, Nucl. Instrum. Methods Phys. Res., Sect. A **499**, 633 (2003).
[33] M. Beddo *et al.*, The STAR barrel electromagnetic calorimeter, Nucl. Instrum. Methods Phys. Res., Sect. A **499**, 725 (2003).
[34] B. Bonner, H. Chen, G. Eppley, F. Geurts, J. Lamas-Valverde, C. Li, W. J. Llope, T. Nussbaum, E. Platner, and J. Roberts, A single Time-of-flight tray based on multigap resistive plate chambers for the STAR experiment at RHIC, Nucl. Instrum. Methods Phys. Res., Sect. A **508**, 181 (2003).
[35] L. Ruan *et al.*, Perspectives of a Midrapidity dimuon program at RHIC: A novel and compact muon telescope detector, J. Phys. G **36**, 095001 (2009).
[36] W. J. Llope *et al.*, The STAR vertex position detector, Nucl. Instrum. Methods Phys. Res., Sect. A **759**, 23 (2014).
[37] J. Kiryluk, Relative luminosity measurement in STAR and implications for spin asymmetry determinations, AIP Conf. Proc. **675**, 424 (2003).
[38] S. Luo, Ph.D. thesis, University of Illinois at Chicago, 2020. https://drupal.star.bnl.gov/STAR/theses/phd-99.
[39] H. Bichsel, A method to improve tracking and particle identification in TPCs and silicon detectors, Nucl. Instrum. Methods Phys. Res., Sect. A **562**, 154 (2006).
[40] R. Brun, F. Bruyant, M. Maire, A. C. McPherson, and P. Zanarini, GEANT3, CERN Report No. CERN-DD-EE-84-1, 1987, https://cds.cern.ch/record/1119728.
[41] M. Tanabashi *et al.* (Particle Data Group), Review of particle physics, Phys. Rev. D **98**, 030001 (2018).
[42] H.-F. Zhang, Z. Sun, W.-L. Sang, and R. Li, Impact of η_c Hadroproduction Data on Charmonium Production and Polarization within Nonrelativistic QCD Framework, Phys. Rev. Lett. **114**, 092006 (2015).
[43] A. Abulencia *et al.* (CDF Collaboration), Polarizations of J/ψ and $\psi(2S)$ Mesons Produced in $p\bar{p}$ Collisions at $\sqrt{s} = 1.96$ TeV, Phys. Rev. Lett. **99**, 132001 (2007).
[44] A. M. Sirunyan *et al.* (CMS Collaboration), Constraints on the χ_{c1} versus χ_{c2} Polarizations in Proton-Proton Collisions at $\sqrt{s} = 7$ TeV, Phys. Rev. Lett. **124**, 162002 (2020).